

Rapid mantle flow with power-law creep explains deformation after the 2011 Tohoku mega-quake

Ryoichiro Agata^{1*}, Sylvain D. Barbot², Kohei Fujita³, Mamoru Hyodo¹, Takeshi Iinuma¹, Ryoko Nakata¹, Tsuyoshi Ichimura³, Takane Hori¹

May 7, 2018

1. Japan Agency for Marine-Earth Science and Technology, Yokohama, Japan.
2. Earth Observatory of Singapore, Asian School of the Environment, Nanyang Technological University, Singapore.
3. Earthquake Research Institute, The University of Tokyo, Tokyo, Japan.

Abstract: The deformation transient that follows large subduction zone earthquakes is thought to originate from the interaction of viscoelastic flow in the asthenospheric mantle and slip on the megathrust that are both accelerated by the sudden coseismic stress change[1]. The surface deformation following the 2011 Mw 9.0 Tohoku earthquake[2, 3, 4, 5] provides some of the most comprehensive constraints on surface deformation following mega-quakes. Assuming that the flow of mantle rocks is Newtonian, the low viscosity required to explain surface deformation was attributed to a weak lithosphere-asthenosphere boundary[4, 6, 7], but these findings are at odds with well-established results from mineral physics[8, 9]. Here, we show that combining insight from laboratory solid-state creep[8, 9] and friction experiments[10, 11] can successfully explain the spatial distribution of surface deformation in the first few years after the Tohoku earthquake[2, 3, 4, 5]. The transient reduction of effective viscosity resulting from power-law (nonlinear) stress-strain-rate interactions in the asthenosphere explains the peculiar reversal of trench-perpendicular displacements revealed by seafloor geodesy, while the rapid slip acceleration on the megathrust accounts for surface displacements on land and offshore outside the rupture area. The low-velocity zone of the lithosphere-asthenosphere boundary has been previously associated with a permanent low-viscosity structure[12]. In contrast, our results suggest that a rapid mantle flow takes place in the lithosphere-asthenosphere boundary with temporarily decreased viscosity in response to large coseismic stress, presumably due to the activation of power-law creep during the postseismic period.

Post-earthquake deformation can be interpreted as a process of relaxing the stress perturbation caused by the earthquake rupture. It generally consists of the deformation due to continued, mostly aseismic slip on the megathrust (afterslip)[13] and viscoelastic relaxation in the asthenosphere [1]. Afterslip relaxes the stress perturbation by localized deformation in the region of the fault plane that surrounds the earthquake rupture. Viscoelastic flow relaxes the coseismic stress change by distributed, plastic deformation in the surrounding mantle [14, 15]. The post-earthquake deformation of the 2011 M_w 9.0 Tohoku-Oki earthquake was captured by a wide array of land-based[16, 2] and seafloor[3, 4, 5] instruments. This widespread observation network captured a complex post-earthquake deformation field. Some near-trench seafloor stations moved seaward, in the opposite direction to the long-term subduction motion, while others moved landward (Fig. 1a). The post-earthquake vertical motion was also complex, with many seafloor stations moving in opposing directions than that on land. Several studies [3, 4, 17, 6, 18] claim that viscoelastic relaxation largely contributed to these patterns.

The 2011 M_w 9.0 Tohoku-Oki earthquake induced a large stress perturbation in the surrounding lithosphere that accelerated the flow in the oceanic asthenosphere and in the mantle wedge. It is natural to expect that viscoelastic relaxation during the post-earthquake period can be described by the constitutive properties of peridotite, a rock assemblage of mostly pyroxene and olivine, under high temperature and pressure conditions. Likewise, afterslip may be described by the frictional properties of the megathrust. Laboratory experiments suggest that the plastic deformation of mantle rocks is accommodated by a thermally activated flow that obeys a power-law relation between stress and strain-rate [9, 8]. The friction between the subducting slab and the upper plate is governed by a laboratory-derived kinematic friction law [10, 11] that predicts the velocity of afterslip based on the stress evolution. Incorporating the laboratory-derived constitutive properties for viscoelastic flow and afterslip successfully explained the deformation that followed the 2012 M_w 8.6 Indian Ocean earthquake [15], for which the surrounding rheological structure is rather simple. In contrast, most studies of the Tohoku-Oki earthquake employed simplified rheological models with linear viscoelastic flow in the mantle and kinematic afterslip [4, 7, 6], or explored more realistic rock properties in two-dimensional models [17, 19]. This limitation of approach is probably due to the difficulty in dealing with the combination of the geometrical complexity and the nonlinear governing equations. All of the linear viscoelastic models inferred from the Tohoku-Oki earthquake includes a thin low-viscosity (weak) layer along the lithosphere–asthenosphere boundary (LAB) in the upper mantle [4, 6, 7]. A sharp decrease of seismic velocity at LAB [12, 20] has been attributed to the presence of water, which upholds the existence of a low-viscosity layer as a permanent rheology structure [4]. This interpretation remains controversial, as recent experiments invalidate high water concentration to explain the low-velocity layer at the lithosphere–asthenosphere boundary [21].

Here, we consider the three-dimensional response of the lithosphere–asthenosphere system following the 2011 M_w 9.0 Tohoku-Oki earthquake with power-law viscoelastic flow in the mantle and afterslip on the megathrust, incorporating a realistic velocity structure for the Japanese margin, Earth’s sphericity and laboratory-derived, nonlinear rock constitutive properties. We assume that the viscoelastic flow of the upper mantle is accommodated by steady-state dislocation creep, with the following stress-strain-rate relationship [9]

$$\dot{\epsilon} = K(C_{\text{OH}})^r \sigma^n \exp\left(-\frac{H}{RT}\right) \quad (1)$$

where $\dot{\epsilon}$ is the norm of the strain-rate tensor, K is a pre-exponential factor, C_{OH} and r are the water concentration and its exponent, σ is the norm of deviatoric stress tensor, n is the stress exponent, $H = Q + p\Omega$ is the activation enthalpy, R is the universal gas constant, T is the temperature. The enthalpy incorporates the activation energy Q and the activation volume Ω and depends on the confining pressure p . As the model already exhibits significant complexity due to the coexistence of viscoelastic flow and afterslip with lateral variations of constitutive properties, and since its constitutive properties are still unclear, we ignore the transient creep that is thought to take place during the early stage of post-earthquake transients [22, 15]. We combine dislocation creep with diffusion creep, but the latter does not play a significant role in our short-term simulations (see Methods). The temperature profile is based on a two-dimensional model for the Tohoku region [23], which we expanded along strike with a mantle temperature of 1380°C (Fig. 1b), compatible with another study [15]. We converted the background shortening rate of 10^{-8} yr^{-1} to determine the background stress based on the rheological law [24]. We assume that the velocity of afterslip on the megathrust is governed by the rate- and state-dependent friction (see Methods for details), given by

$$V = V_* \exp\left(\frac{\tau - (\tau_{s*} + \Delta\tau_s)}{A}\right), \quad (2)$$

where τ is the shear traction, τ_{s*} is the steady-state frictional resistance, $\Delta\tau_s$ is a state variable [25]. A is a parameter that controls the fracture energy consumed during fault slip. For the initial condition of the simulation, we borrow the coseismic slip (Fig. 1a) and the fault constitutive properties (Fig. 1c

and Extended Data Fig. 5b) from a simulation of giant earthquakes in the Tohoku region [26]. We divide the region into three plates: a continental plate that includes the North-American and Eurasian plates and two oceanic plates, the Pacific and the Philippine Sea plates. Each tectonic plate consists of an elastic layer near the surface (the crust and the lithospheric mantle) and a viscoelastic mantle layer below (Fig. 1c and Fig. 2). The elastic and viscoelastic layers in the three plates share the same elastic properties (Fig. 1c). Simulating the dynamics of this nonlinear system in three-dimensions with realistic elastic, frictional, and viscoelastic properties requires state-of-the-art modeling strategies [27, 28] (see Methods).

Our simulated deformation shows similar patterns to the observation data for the cumulative 2.8 year post-earthquake displacement in the horizontal direction (Fig. 3a) when we choose the following rock properties $K = 10^{0.56} \text{ MPa}^{-n}/\text{s}$, $C_{\text{OH}}=1,000 \text{ ppm H/Si}$, $Q=430 \text{ kJ/mol}$, $r=1.2$, $\Omega=13.5 \text{ cm}^3/\text{mol}$ and $n=3$ (see Methods). For simplicity, we assumed a similar average water content in the oceanic asthenosphere and in mantle wedge, even though water concentration may be large in the mantle wedge corner due to slab dehydration [29]. The values adopted for the activation energy and the activation volume fall well within the uncertainties constrained by laboratory experiments [8], e.g., $Q = 410 \pm 50 \text{ kJ/mol}$ and $\Omega = 11 \pm 3 \text{ cm}^3/\text{mol}$, despite the required extrapolation to different temperature and pressure conditions. This indicates that the physical and geological setting of the Japan subduction zone is understood well enough to make accurate predictions about how the lithosphere-asthenosphere system will deform in response to a large earthquake.

The temporal and spatial evolution of effective viscosity after the giant earthquake naturally results from the nonlinear constitutive relation (1) and plays an important role in the rapid and complex deformation that occurs during the post-earthquake period. In response to the large (above 1 MPa) stress perturbation in the upper mantle, the effective viscosity (see Methods) was largely reduced shortly after the earthquake in the depth of 80-180 km in the oceanic mantle and 100-200 km in the mantle wedge (Fig. 4). The flow of low-viscosity mantle material below the trench axis drives westward motion around the trench, explaining the continued displacement of the seafloor stations located above the coseismic rupture (MYGI, KAMS and KAMN, Fig. 3b). The accelerated flow in the mantle wedge contributes to the eastward displacement of GPS stations on land. Afterslip on the megathrust is essential to explaining the deformation on land, but also the spatial pattern of displacement of the seafloor stations, such as eastward displacement seen in the stations FUKU and MYGW (Fig. 3b). Both these stations are in locations where viscoelastic flow produces little horizontal displacement, making the post-earthquake response due to the afterslip dominant there (Fig. 4).

Remarkably, the spatial distribution of effective viscosity derived from laboratory data and coseismic stress change is similar to those inferred from optimization of simplified linear viscoelastic models [4, 6, 7]. The effective viscosity shortly after the earthquake is around $2 \times 10^{17} \text{ Pa s}$ at the minimum both in mantle wedge and oceanic mantle. This is equivalent to the viscosity in a linear transient creep model that fits observed post-earthquake deformation during the early stage [4]. The LAB, originally identified as a low-seismic-velocity layer [12, 20], has also been associated with a permanent low-viscosity structure. However, our result suggests that the LAB hosts a rapid mantle flow with temporarily decreased viscosity in response to large coseismic stress, rather than has a permanent low-viscosity layer. This is consistent with the recent finding that implies the presence of water does not support there exists a low-velocity structure [21].

Despite the excellent fit at numerous stations in the far-field, there remain a few discrepancies with the near-field data, presumably because our model does not include some details of the coseismic rupture offshore. For example, the simulated horizontal displacement at the station FUKU is nearly half of the measured one, despite a good agreement in the azimuthal direction. A peak of the amplitude of afterslip in the green ellipse in Fig. 3b should be slightly closer to station FUKU to fit the data, perhaps indicating that the coseismic slip was overestimated in this region. Such afterslip distribution should also fit better the horizontal displacements in the southern part of the land area (the purple ellipse in Fig. 3a). In the vertical displacement, significant uplift is observed in the fore-arc (The purple circles in Fig. 4). In the trench-normal profile of the stations MYGI and MYGW, although viscoelastic flow in the simulation produces uplift in this region, subsidence due to the afterslip cancels

it out (the green circles in Fig. 4). Furthermore, a significant portion of this uplift in viscoelastic flow is due to stress change associated with afterslip, which we inferred from simulations of viscoelastic flow that exclude afterslip (the green circles in Extended Data Fig. 8a). Without the interaction between afterslip and viscoelastic flow, the computed 2.8-year horizontal displacements are reduced by more than 10% in some of the land stations, and the vertical ones change by more than 30% in many stations in both the land and the seafloor (Extended Data Fig. 8b). As afterslip in the near field can be highly sensitive to the details of the coseismic rupture, these residuals may be caused by still unresolved slip patterns of the mainshock. Despite these shortcomings, our results highlight the nonlinear interactions among coseismic slip, afterslip and viscoelastic flow.

Our study demonstrates that a rheological model of the plate boundary based on independent geological and geophysical data can make realistic, first-order predictions of the transient response of the lithosphere following giant earthquakes. Complex post-earthquake deformation of a large subduction zone earthquake can be well explained by taking into account the laboratory-derived friction and viscoelastic flow laws in a three-dimensional structural model. The discrepancy between the simulation and the data should be reduced, in principle, by refined models of the coseismic rupture and the in situ conditions such as initial stress, temperature and confining pressure, properties that are usually constrained for long time scales [23, 30]. The approach is generally applicable to other ocean-continent subduction zones, implying that our understanding of viscoelastic properties and rocks friction may be detailed enough to predict the slow deformation of the lithosphere during the postseismic and interseismic periods.

Methods

0.1 Rheology model for upper mantle

We used the dislocation creep model based on the laboratory-derived power-law relation and the linear Maxwell element in series:

$$\dot{\epsilon} = K(C_{\text{OH}})^r \sigma^n \exp\left(-\frac{Q + p\Omega}{RT}\right) + \frac{1}{2\eta_l} \sigma, \quad (3)$$

where η_l is a constant value for viscosity in the linear Maxwell element. This simplifies the treatment of diffusion creep, based on the idea that viscosity in diffusion creep is 10^{1-2} times larger than effective viscosity in dislocation creep shortly after earthquakes of M_w 8.2 and 8.6[15], and the influence of diffusion creep is not expected to be very large in the 2.8 years deformation after the 2011 M_w 9.0 Tohoku-Oki earthquake. We use $\eta_l = 1 \times 10^{19}$ Pa s for the whole of the region, which is nearly the average value of the viscosity structure estimated for steady state 2D model around the Japan Trench[24]. In tensor notation,

$$\dot{\epsilon}_{ij} = K(C_{\text{OH}})^r |\sigma'_{ij}|^{n-1} \exp\left(-\frac{Q + p\Omega}{RT}\right) \sigma'_{ij} + \frac{1}{2\eta_l} \sigma'_{ij}, \quad (4)$$

where the apostrophe denotes deviatoric tensor, and $|\cdot|$ is the norm of tensor (square root of the second invariant of the tensor). We defined effective viscosity to be $\eta_{\text{eff}} = \sigma/2\dot{\epsilon}$, thus

$$\eta_{\text{eff}} = \frac{\eta_p \eta_l}{\eta_p + \eta_l} \quad (5)$$

where

$$\eta_p = \frac{1}{2K(C_{\text{OH}})^r} |\sigma'_{ij}|^{-n+1} \exp\left(\frac{Q + p\Omega}{RT}\right). \quad (6)$$

Our temperature pattern (Fig. 1b) in the elastic slab is significantly different from the reference thermal model[23] in that it keeps a low temperature even in the depth deeper than 200 km. However, it affects little the simulation results because high pressure is dominant and does not affect much viscoelastic

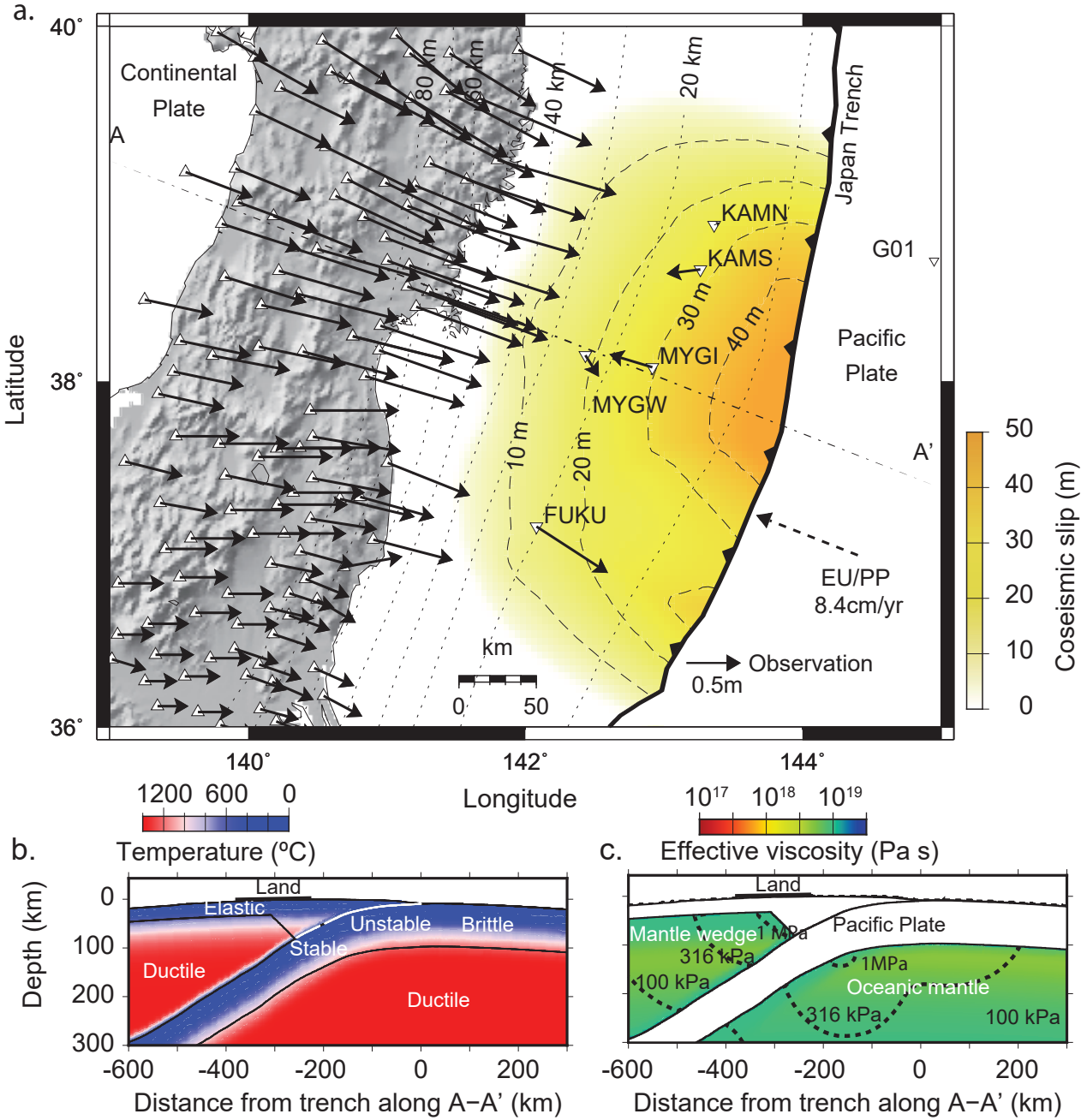


Figure 1: Post-earthquake deformation 2.8 years after the 2011 Tohoku-Oki Earthquake and surrounding material properties. a, Measured displacement in the land stations [16, 2] (triangles) and the seafloor stations [3, 5] (inverse triangles). We removed some land stations for visibility. Coseismic displacement is not available in the station G01. Dashed-dotted and dotted lines are the location of the cutting plane (A-A' profile) and the depth of the plate boundary, respectively. b, Assumed temperature structure and frictional properties in the A-A' profile. In the “unstable” region, where coseismic slip is input in our simulation, friction parameters are set as $-0.2 \text{ MPa} \leq A - B \leq -0.1 \text{ MPa}$ and $0.2 \text{ m} \leq L \leq 0.3 \text{ m}$. In the “stable” region, where afterslip occurs in our simulation, $A - B = 0.1 \text{ MPa}$ and $L = 13 \text{ m}$ (also see Extended Data Fig. 5b). The temperature values in the layers of elastic materials are not used in the simulation. c, The assumed viscoelastic structure and the stress change along the A-A' profile. The mantle wedge and oceanic mantle are viscoelastic with $\mu_v = 65 \text{ GPa}$. The remaining volume is elastic with $\mu_e = 45 \text{ GPa}$. Poisson's ratio is $\nu = 0.25$ and density is $\rho = 3300 \text{ kg m}^{-3}$ everywhere. The color indicates the effective viscosity before the earthquake and the computed stress distribution. Contribution from dislocation creep is dominant in the area with the light yellow, while viscosity in the linear term is dominant (see Methods) elsewhere. The dashed contour line indicates summation of background stress and coseismic stress (norm of deviatoric stress tensor).

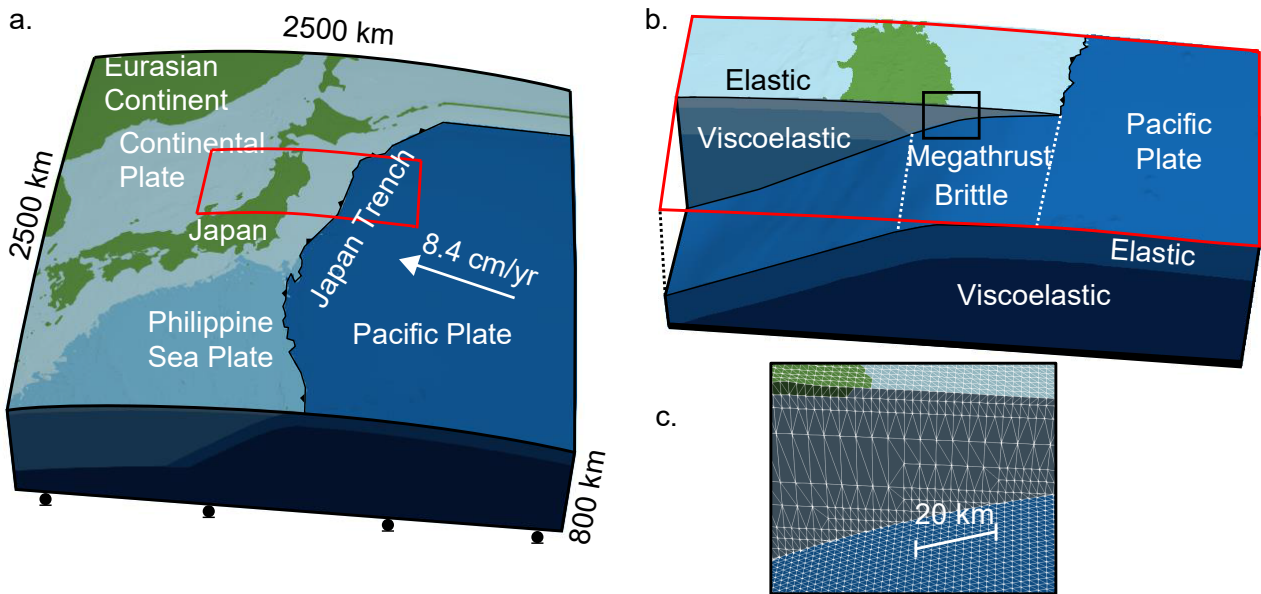


Figure 2: The finite-element model used in our study. **a.** Overview, **b.** close-up view for the region of the red rectangular in **a** with the location of the megathrust and **c.** close-up view for the region of the yellow rectangular in **b** with finite-element mesh patterns. The elements with the same color are in the same structural component (we have six of them, elastic and viscoelastic layer in three plates). The green color is used to distinguish the elements that are located above the sea level. The green elements have the same material properties as those in the continental plate.

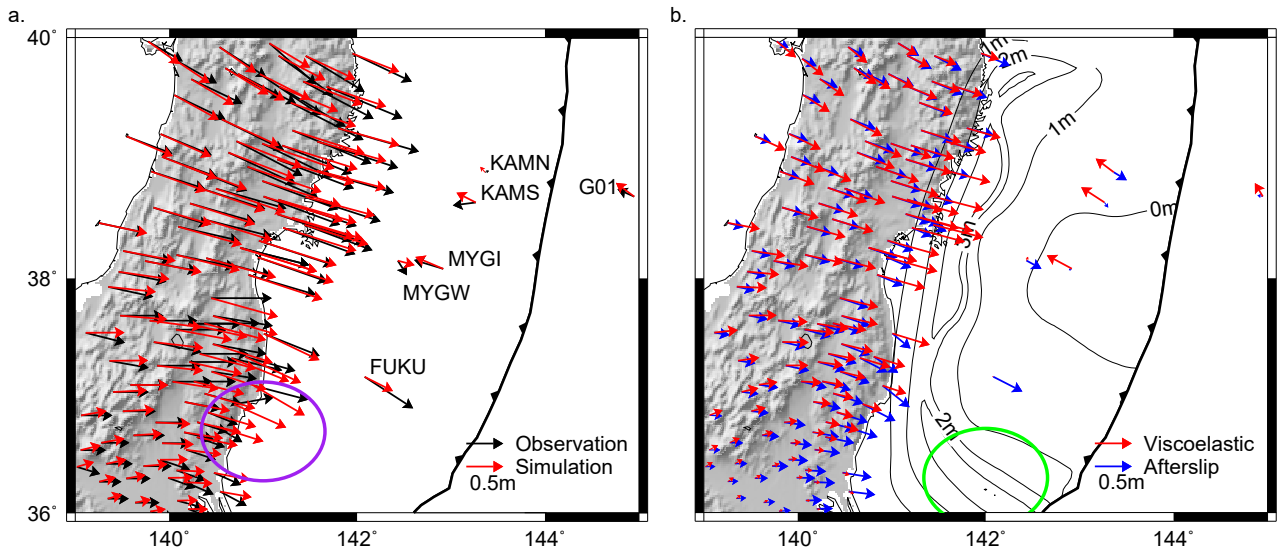


Figure 3: Post-earthquake deformation of the 2011 Tohoku-Oki earthquake. a, The horizontal component of 2.8-year post-earthquake displacements. In the station G01, displacement in the period 1.5 years and 2.8 years after the earthquake is plotted because of the limitation of data availability. In addition, the contribution from the plate convergence rate (shown in Fig. 1a), which is not included in our simulation scheme, is added to the simulation result in the station. b, The horizontal components of 2.8-year post-earthquake displacements in the simulation broken down into the contribution from afterslip and viscoelastic flow. The viscoelastic component includes the contribution from both coseismic slip and afterslip. The contour lines indicate accumulated afterslip for 2.8 years. A peak of the amplitude of afterslip in the green ellipse should be slightly closer to the station FUKU to fit better the horizontal displacements in FUKU and the purple ellipse.

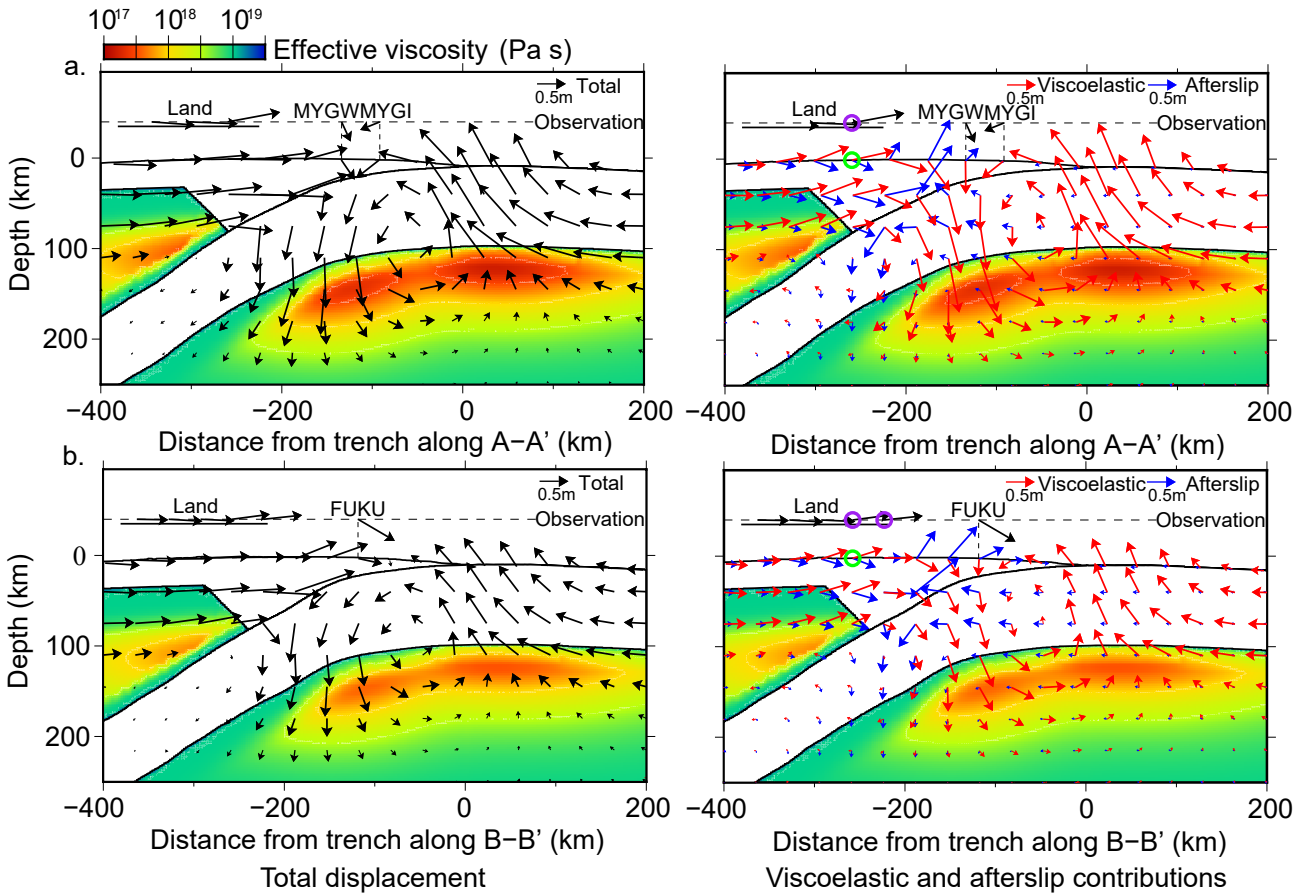


Figure 4: Simulation results on the cutting planes that are parallel to plate convergence direction, going through seafloor stations (a: the A-A' profile with MYGW and MYGI, b: the B-B' profile, which is parallel to A-A' and runs by the station FUKU). The figures on the left are for the total displacement after 2.8 years. The panels on the right show the contribution from afterslip and viscoelastic flow after 2.8 years. The color indicates the distribution of effective viscosity due to coseismic stress change. The black arrows on the horizontal dashed line are the observed displacements. In the location of purple circles, observation data shows uplift, while in the green circles, computed uplift viscoelastic displacement is canceled out by subsidence due to afterslip.

flow in this depth. In the simulation, we use the values proposed from laboratory experiments[8] for K , r and n , while Q and Ω were chosen within the error bar obtained in the same experiments, so that the computed displacement values are more consistent with the data. We set the C_{OH} value as an average in the upper mantle. Further study on more detailed variation of measured displacement should require considering heterogeneous distribution of water content[15, 31].

0.2 Coseismic slip and fault friction setting

To compute post-earthquake deformation, we take over an M9-class earthquake scenario calculated in an earthquake cycle simulation in the Tohoku region carried out by Nakata *et al.*[26]. This simulation supposes that space-time variations in slip velocity are assumed to be a slip with a frictional interface. We assume that equilibrium equation in shear stress on the fault plane, which is described as,

$$\frac{d\tau_i}{dt} = F_i(\mathbf{V} - \mathbf{V}_{pl}, \dot{\boldsymbol{\epsilon}}^{\text{inelastic}}) - \gamma \frac{dV_i}{dt} \quad (7)$$

where τ_i and V_i are shear stress and slip velocity on a FEM node i on the fault. V_i is in the direction opposite to the convergence rate (Fig. 1). \mathbf{V} and \mathbf{V}_{pl} are vectors whose components are V_i and V_{pli} , the plate convergence rate. $V_{pl} = 8.4\text{cm/yr}$ is used for the whole region in this study. $\boldsymbol{\epsilon}^{\text{inelastic}}$ is inelastic strain in the targeted 3D body. The second term introduces the effect of the seismic radiation damping[32]. We use $\gamma = 0.3\mu/2c$, which is used in Nakata *et al.*[26] to reproduce a shorter duration during the 2011 Tohoku-Oki earthquake[33], where μ is the rigidity and c is the shear wave velocity. In many studies the simulations with elastic homogeneous half-space have been carried out, where $\dot{\boldsymbol{\epsilon}}^{\text{inelastic}} = 0$. This makes F_i a linear function of \mathbf{V} and enable F_i to be discretized by the boundary integral equation method (BIEM). In this study, we evaluate F_i directly by using the finite element method (see Section 0.3), in which F_i can be a function of both \mathbf{V} and $\dot{\boldsymbol{\epsilon}}^{\text{inelastic}}$, and arbitrary geometry and material heterogeneity can be considered. It should be noted that a BIEM approach that can incorporate inelastic strain in elastic homogeneous half-space was proposed recently[34]. The rate- and state-dependent friction law is used to model frictional behavior on the plate interface as

$$V_i = V_* \exp\left(\frac{\tau_i - (\tau_{s*i} + \Delta\tau_{si})}{A_i}\right), \quad (8)$$

$$\frac{d\Delta\tau_{si}}{dt} = \frac{B_i}{L_i/V_*} \exp\left(-\frac{\Delta\tau_{si}}{B_i}\right) - \frac{B_i V_i}{L_i}. \quad (9)$$

(8) represents a fault constitutive law that determines V_i for a given τ_i and a value of $\tau_{si}(=\tau_{s*i} + \Delta\tau_{si})$, where $\Delta\tau_{si}$ is a state variable which is analogous to the ‘‘strength as a threshold’’[25] and τ_{s*i} the steady state strength with $V_i = V_{pl}$. (9) is an aging law[11]. The frictional parameter B controls strength recovery, while L controls slip weakening. Time integration is performed using an adaptive time step fifth-order Runge-Kutta algorithm[35]. In our simulation, initial value of τ_i and $\Delta\tau_{si}$ is extracted from a time step right after the earthquake in the simulation of Nakata *et al.*[26](Extended Data Fig. 5a). The values are multiplied by 0.7, because the coseismic slip computed in their simulation fits best the coseismic crustal deformation data when multiplied by 0.7 (mentioned in the next paragraph). The initial value of V_i is calculated with (8). Frictional parameters are also the same as in Nakata *et al.*[26], excluding that small patches for M7 earthquakes are removed (Extended data Fig. 5b).

Extended Data Fig. 6 shows the coseismic slip, the same as in Fig. 1, which we extracted from the cycle simulation results, and comparison between computed and observed coseismic displacement. Although this slip model is not inferred from observation data, it fits the horizontal component of coseismic crustal deformation data well when multiplied by 0.7. The stress distribution computed in response to this coseismic slip is used as the stress perturbation to compute power-law viscoelastic flow and afterslip evolution.

0.3 Finite-element modeling

In the finite-element modeling, we discretize the equations for viscoelastic deformation and fault friction using the mesh shown in Fig. 2. The mesh was constructed using an updated version of

a meshing technique for quadratic tetrahedral elements based on a background structured grid[28]. In the method, at first a uniform background cell covering entire targeted domain was used, and it defined the resolution of the layer interfaces as ds . The geometries of the ground surface and interfaces were simplified slightly to maintain good element quality. At the same time, unnecessary elements were merged to generate larger elements elsewhere. This method enables automated and robust construction of high-resolution tetrahedral mesh directly from digital elevation model (DEM) data of crustal structure without creating a CAD (computer-aided design) model. The updated version of the meshing algorithm carries out an additional post process to minimize the simplification of the geometry in the ground surface and interfaces as much as possible. Input elevation data sets are based on 900 m resolution topography data (JTOPO30), the CAMP model[36] and a velocity data set for the Japanese Island[37]. With $ds = 2$ km and little simplification of the geometry, shear stress distribution on the fault, which is essential for computing stress-driven afterslip, is evaluated accurately in the target problem. The finite element mesh has 1,402,810,116 degree-of-freedom (DOF) and 346,885,129 tetrahedral elements. In viscoelastic material and elastic material, rigidity is $\mu_v = 65$ GPa and $\mu_e = 45$ GPa, respectively. Poisson’s ratio is $\nu = 0.25$ and density is $\rho = 3300$ kg m⁻³ everywhere. This setting follows Sun et al. (2014)[4].

To evaluate F_i in (7), we applied an algorithm based on a viscoelastic finite element formulation[38, 39], which we modified to consider nonlinear viscoelasticity. Slip velocity \mathbf{V} is input to the finite-element model using the split node technique[40] to evaluate response displacement rate. We consider the effect of gravity using surface gravity approximation[41]. Since no inertia term is included in the equations, the problem is quasi-static, which ends up with solving an elliptic problem in every time step. It means we need to solve the system which has billions of DOF. We introduced a modified version[42] of a massively-parallel FEM solver for computing crustal deformation[28] based on “GAMERA”[27] (a physics-based seismic wave amplification simulator, enhanced by a multi-Grid method, Adaptive conjugate gradient method, Mixed precision arithmetic, Element-by-element method, and pRedictor by Adams-Bashforth method).

We run the calculation using 2048 computer nodes (16384 computer cores) of the K computer at RIKEN, Advanced Institute for Computational Science[43], each computer node of which has one CPU (Fujitsu SPARC64 VIIIfx 8 core 2.0 GHz) and 16 GB of memory, for 7.5 hours to obtain the post-earthquake deformation for 2.8 years shown in Fig 3.

0.4 Viscoelastic and afterslip contributions

Fig. 3b and the figures in the right in Fig. 4 present breakdown of computed displacement into contribution from viscoelastic flow and afterslip. This is calculated in the following manner:

1. Extract accumulated 2.8 year afterslip distribution that is computed based on the nonlinear interaction of the rate- and state-dependent friction law and the nonlinear rock constitutive properties in the original simulation.
2. Compute elastic response displacement $\mathbf{u}_{\text{afterslip}}$ due to the extracted afterslip. $\mathbf{u}_{\text{afterslip}}$ corresponds to the blue arrows in Fig. 3 and 4.
3. $\mathbf{u}_{\text{viscoelastic}} = \mathbf{u}_{\text{original}} - \mathbf{u}_{\text{afterslip}}$, where $\mathbf{u}_{\text{viscosity}}$ and $\mathbf{u}_{\text{original}}$ correspond to the red and black arrows in Fig. 3 and 4, respectively.

We also present a result post-earthquake deformation simulation with “no interaction” between viscoelastic flow and afterslip (Extended Data Fig 8). In this simulation, we computed viscoelastic flow without the friction law (the red arrows in Extended Data Fig 8a), while computing afterslip without the nonlinear rock constitutive properties, only with pure elasticity. We finally summed up these to compute total deformation without their interaction (the red arrows in Extended Data Fig 8b).

Acknowledgement This study was partially supported by JSPS Fellowship (26-8867). We obtained the results using the K computer at the RIKEN Advanced Institute for Computational Science

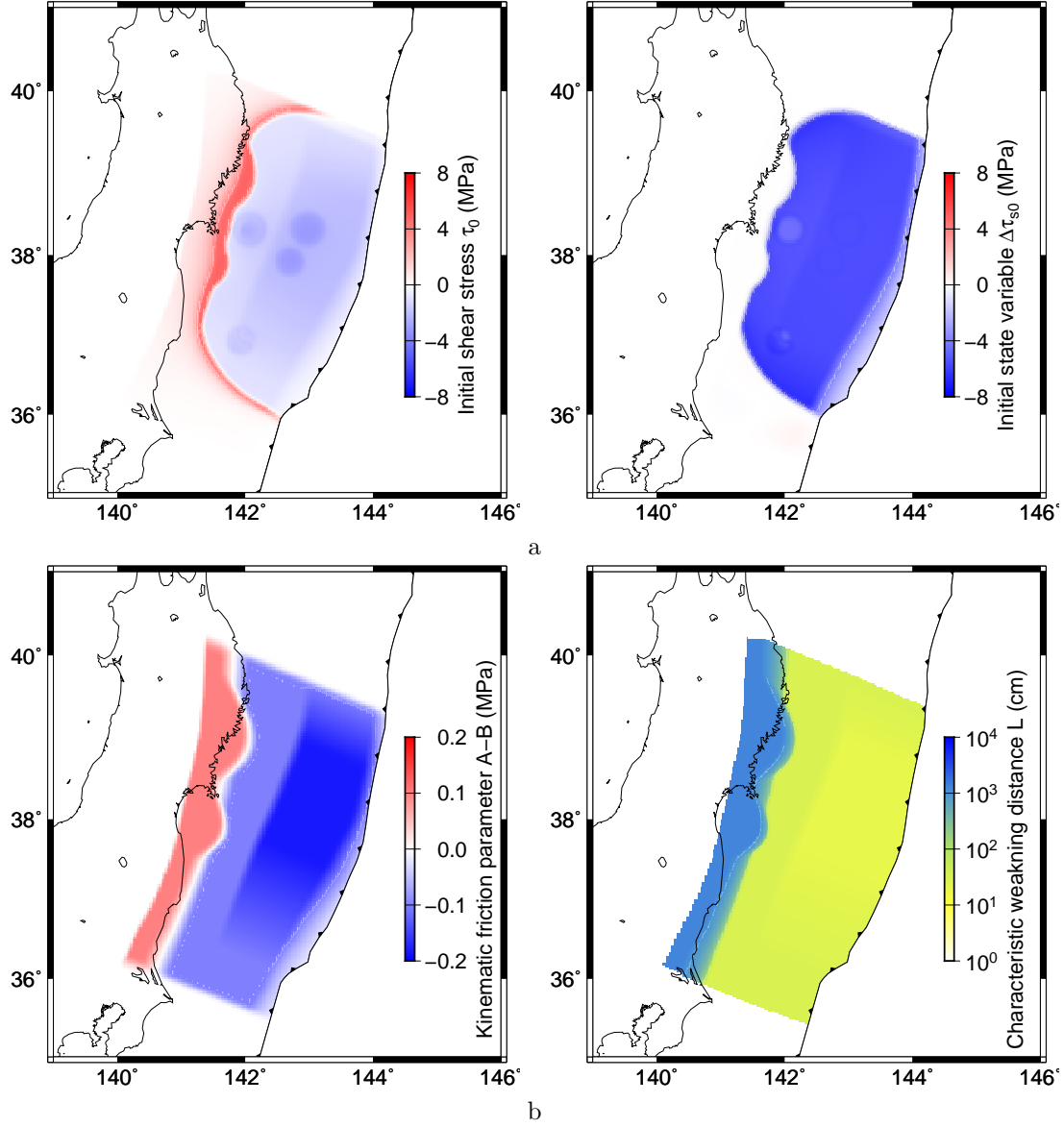


Figure 5: (Extended Data) The variables and parameters taken over from Nakata et al.[26]. a, Shear stress and state variable. Initial value of slip velocity V_i is calculated using these values with (8). b, Frictional parameters.

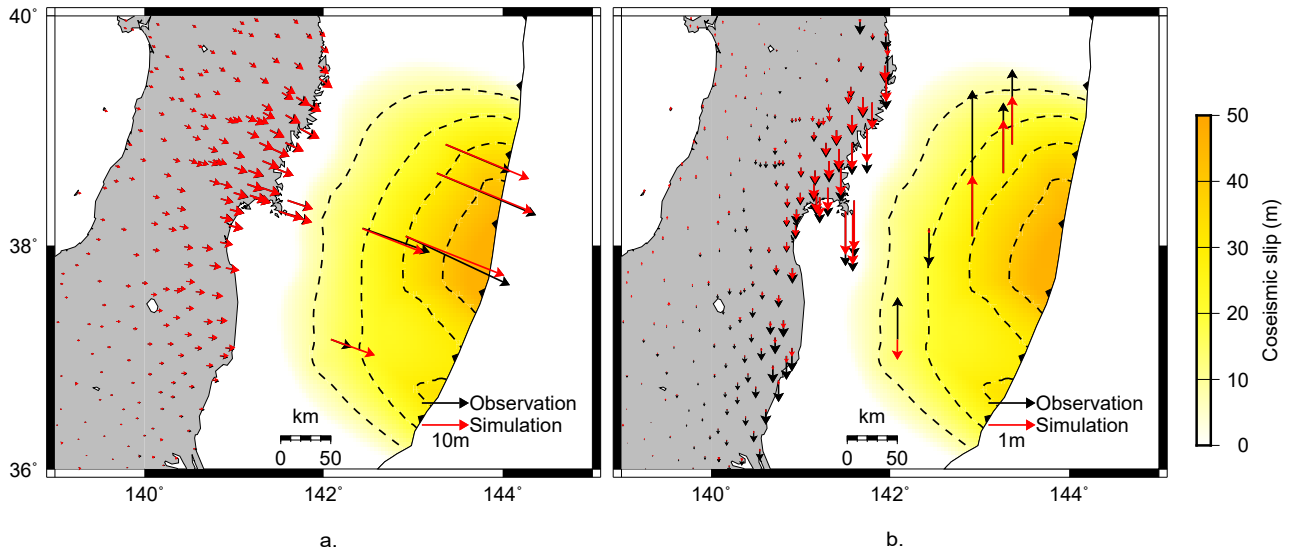


Figure 6: (Extended Data) Input coseismic slip based on Nakata *et al.*[26] and comparison between computed and observed coseismic displacement, including both the land[16, 44] and seafloor stations[45].

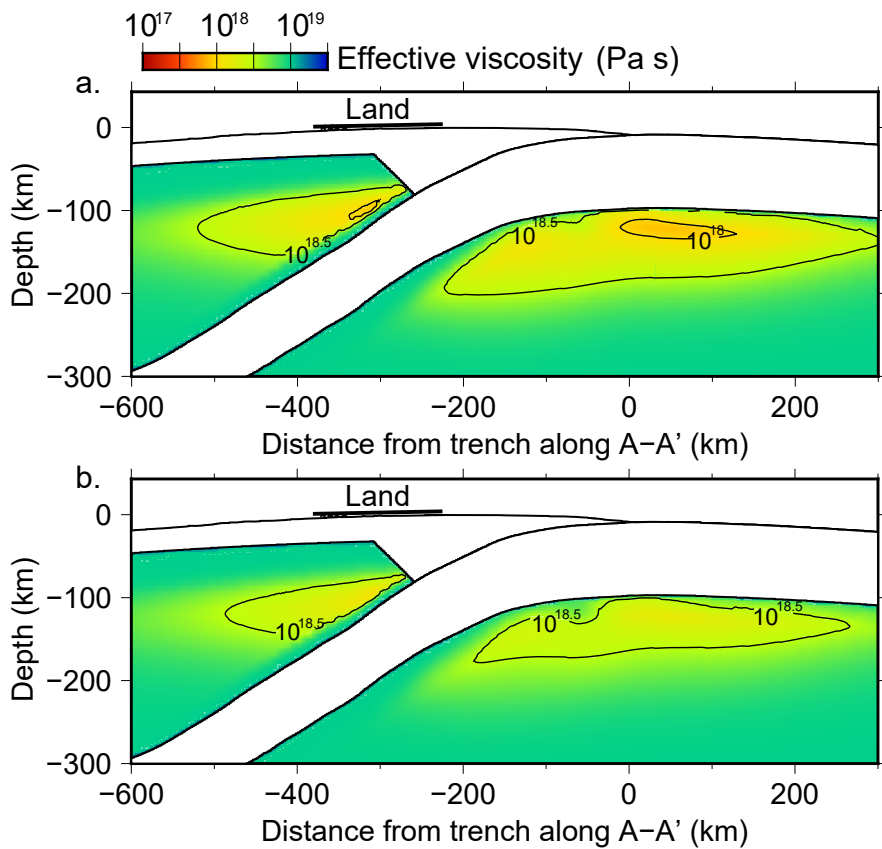


Figure 7: (Extended Data) Distributions of effective viscosity at a, 1 year and b, 2.8 years after the earthquake. The distribution of viscosity varies with time.

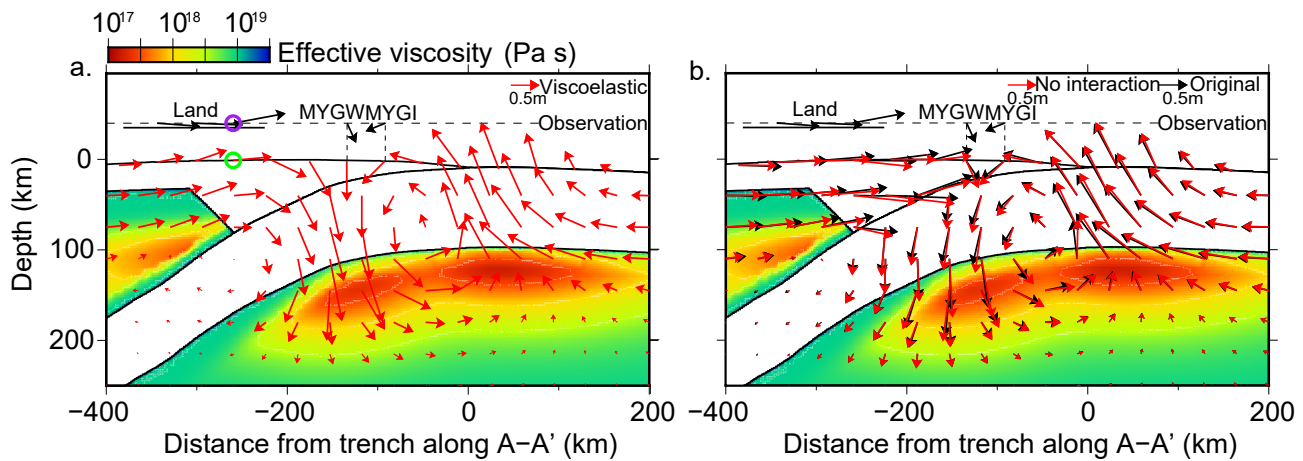


Figure 8: (Extended Data) a, Power-law viscoelastic flow in 2.8 years without considering afterslip in the cutting plane of the station MYGI and MYGW. In the green circle, uplift is significantly smaller than in the case with afterslip, shown in Fig. 4a. b, Comparison between the total 2.8-year displacement in the original simulation (black, the same as "total" in Fig. 4) and the result without interaction between afterslip and viscoelastic flow (red). As a result, the computed horizontal displacements are reduced by more than 10% in some of the land stations, and the vertical ones change by more than 30% in many stations in both of the land and the seafloor.

(Proposal number hp160221 and hp170249). This work was supported by Post K computer project (Priority issue 3: Development of Integrated Simulation Systems for Hazard and Disaster Induced by Earthquake and Tsunami).

Author Contributions R.A. and T.H. designed and conducted the study. R.A, S.D.B. and T.H. wrote the manuscript. R.A., K.F. and T. Ichimura wrote the simulation code. S.D.B. and M.H. contributed to refining the simulation algorithm. S.D.B. and T. Inuma contributed to the modeling. R.N. prepared data for afterslip calculation.

Materials & Correspondence Correspondence and requests for materials should be addressed to R.A. (email: agatar@jamstec.go.jp).

References

- [1] Wang, K., Hu, Y. & He, J. Deformation cycles of subduction earthquakes in a viscoelastic Earth. *Nature* **484**, 327–32 (2012). URL <http://www.ncbi.nlm.nih.gov/pubmed/22517160>.
- [2] Ozawa, S. *et al.* Coseismic and postseismic slip of the 2011 magnitude-9 Tohoku-Oki earthquake. *Nature* **475**, 373–376 (2011). URL <http://www.ncbi.nlm.nih.gov/pubmed/21677648>.
- [3] Watanabe, S. *et al.* Evidence of viscoelastic deformation following the 2011 Tohoku-oki earthquake revealed from seafloor geodetic observation. *Geophysical Research Letters* (2014). URL <http://doi.wiley.com/10.1002/2014GL061134>.
- [4] Sun, T. *et al.* Prevalence of viscoelastic relaxation after the 2011 Tohoku-oki earthquake. *Nature* **514**, 84–87 (2014). URL <http://www.nature.com/doi/10.1038/nature13778>.
- [5] Tomita, F. *et al.* First measurement of the displacement rate of the pacific plate near the japan trench after the 2011 tohoku-oki earthquake using gps/acoustic technique. *Geophysical Research Letters* **42**, 8391–8397 (2015).

- [6] Freed, A. M. *et al.* Resolving depth-dependent subduction zone viscosity and afterslip from postseismic displacements following the 2011 tohoku-oki, japan earthquake. *Earth and Planetary Science Letters* **459**, 279–290 (2017).
- [7] Suito, H. Importance of rheological heterogeneity for interpreting viscoelastic relaxation caused by the 2011 tohoku-oki earthquake. *Earth, Planets and Space* **69**, 21 (2017).
- [8] Karato, S. & Jung, H. Effects of pressure on high-temperature dislocation creep in olivine. *Philosophical Magazine* **83**, 401–414 (2003).
- [9] Hirth, G. & Kohlstedt, D. Rheology of the upper mantle and the mantle wedge: A view from the experimentalists. *Inside the subduction Factory* 83–105 (2003).
- [10] Dieterich, J. H. Modeling of rock friction: 1. experimental results and constitutive equations. *Journal of Geophysical Research: Solid Earth* **84**, 2161–2168 (1979).
- [11] Ruina, A. Slip instability and state variable friction laws. *Journal of Geophysical Research: Solid Earth* **88**, 10359–10370 (1983).
- [12] Kawakatsu, H. *et al.* Seismic evidence for sharp lithosphere-asthenosphere boundaries of oceanic plates. *Science* **324**, 499–502 (2009).
- [13] Hsu, Y.-J. *et al.* Frictional afterslip following the 2005 nias-simeulue earthquake, sumatra. *Science* **312**, 1921–1926 (2006).
- [14] Freed, A. M. & Bürgmann, R. Evidence of power-law flow in the mojave desert mantle. *Nature* **430**, 548–551 (2004).
- [15] Masuti, S., Barbot, S. D., Karato, S., Feng, L. & Banerjee, P. Upper-mantle water stratification inferred from observations of the 2012 indian ocean earthquake. *Nature* **538**, 373–377 (2016).
- [16] Miyazaki, S. & Y., H. The outlines of the geonet in japanese. *Meteorol. Res. Note* **192**, 105–131 (1998).
- [17] Muto, J. *et al.* Heterogeneous rheology controlled postseismic deformation of the 2011 Tohoku-Oki earthquake. *Geophysical Research Letters* **43**, 4971–4978 (2016).
- [18] Noda, A., Takahama, T., Kawasato, T. & Matsu'ura, M. Interpretation of offshore crustal movements following the 2011 tohoku-oki earthquake by the combined effect of afterslip and viscoelastic stress relaxation. *Pure and Applied Geophysics* **175**, 559–572 (2018).
- [19] Sobolev, S. V. & Muldashev, I. A. Modeling Seismic Cycles of Great Megathrust Earthquakes Across the Scales With Focus at Postseismic Phase. *Geochemistry, Geophysics, Geosystems* **18** (2017). URL <http://doi.wiley.com/10.1002/2017GC007230>.
- [20] Rychert, C. A. & Shearer, P. M. A global view of the lithosphere-asthenosphere boundary. *Science* **324**, 495–498 (2009).
- [21] Cline II, C. J., Faul, U. H., David, E. C., Berry, A. J. & Jackson, I. Redox-influenced seismic properties of upper-mantle olivine. *Nature* **555**, 355 (2018). URL <http://dx.doi.org/10.1038/nature25764>{\%}0Ahttp://10.0.4.14/nature25764.
- [22] Freed, A. M., Herring, T. & Bürgmann, R. Steady-state laboratory flow laws alone fail to explain postseismic observations. *Earth and Planetary Science Letters* **300**, 1–10 (2010).
- [23] Syracuse, E. M., van Keken, P. E. & Abers, G. A. The global range of subduction zone thermal models. *Physics of the Earth and Planetary Interiors* **183**, 73–90 (2010).

- [24] Muto, J. *et al.* Two-dimensional viscosity structure of the northeastern Japan islands arc-trench system. *Geophysical Research Letters* **40**, 4604–4608 (2013). URL <http://doi.wiley.com/10.1002/grl.50906>.
- [25] Nakatani, M. Conceptual and physical clarification of rate and state friction: Frictional sliding as a thermally activated rheology **106** (2001).
- [26] Nakata, R., Hori, T., Hyodo, M. & Ariyoshi, K. Possible scenarios for occurrence of M \sim 7 interplate earthquakes prior to and following the 2011 tohoku-oki earthquake based on numerical simulation. *Scientific reports* **6** (2016).
- [27] Ichimura, T. *et al.* Physics-based urban earthquake simulation enhanced by 10 . 7 BlnDOF \times 30 K time-step unstructured FE non-linear seismic wave simulation. *SC14: International Conference for High Performance Computing, Networking, Storage and Analysis* 15–26 (2014).
- [28] Ichimura, T. *et al.* An elastic/viscoelastic finite element analysis method for crustal deformation using a 3–D island-scale high-fidelity model. *Geophysical Journal International* **206**, 114–129 (2016).
- [29] Ji, Y., Yoshioka, S. & Matsumoto, T. *Journal of Geophysical Research : Solid Earth* 4458–4482 (2016).
- [30] Morishige, M. & van Keken, P. E. Along-arc variation in the 3–D thermal structure around the junction between the japan and kurile arcs. *Geochemistry, Geophysics, Geosystems* **15**, 2225–2240 (2014).
- [31] Horiuchi, S. S. & Iwamori, H. A consistent model for fluid distribution, viscosity distribution, and flow-thermal structure in subduction zone. *Journal of Geophysical Research: Solid Earth* **121**, 3238–3260 (2016).
- [32] Rice, J. R. Spatio-temporal complexity of slip on a fault. *Journal of Geophysical Research: Solid Earth* **98**, 9885–9907 (1993).
- [33] Thomas, M. Y., Lapusta, N., Noda, H. & Avouac, J.-P. Quasi-dynamic versus fully dynamic simulations of earthquakes and aseismic slip with and without enhanced coseismic weakening. *Journal of Geophysical Research: Solid Earth* **119**, 1986–2004 (2014).
- [34] Lambert, V. & Barbot, S. Contribution of viscoelastic flow in earthquake cycles within the lithosphere-asthenosphere system. *Geophysical Research Letters* **43**, 10,142–10,154 (2016).
- [35] Press, W. H., Teukolsky, S. A., Vetterling, W. T. & Flannery, B. P. *Numerical Recipes in C (2nd Ed.): The Art of Scientific Computing* (Cambridge University Press, New York, NY, USA, 1992).
- [36] Hashimoto, C., Fukui, K. & Matsu’ura, M. 3-D Modelling of Plate Interfaces and Numerical Simulation of Long-term Crustal Deformation in and around Japan. *Pure and Applied Geophysics* **161**, 2053–2068 (2004). URL <http://link.springer.com/10.1007/s00024-004-2548-8>.
- [37] Koketsu, K., Miyake, H., Fujiwara, H. & Hashimoto, T. Progress towards a japan integrated velocity structure model and long-period ground motion hazard map. *Proceedings of the 14th World conference on earthquake engineering* S10–038 (2008).
- [38] Parker, J. *et al.* Geophysical Finite-Element Simulation Tool (GeoFEST): Algorithms and Validation for Quasistatic Regional Faulted Crust Problems. *Pure and Applied Geophysics* **165**, 497–521 (2008). URL <http://link.springer.com/10.1007/s00024-008-0325-9>.
- [39] Hughes, J. R. & Taylor, R. L. Unconditionally stable algorithms for quasi-static elastovisco-plastic finite element analysis. *Computers & Structures* **8**, 169–173 (1978).

- [40] Melosh, H. & Raefsky, A. A simple and efficient method for introducing faults into finite element computations. *Bulletin of the Seismological Society of America* **71**, 1391–1400 (1981). URL <http://www.bssaonline.org/content/71/5/1391.short>.
- [41] Segall, P. *Earthquake and volcano deformation* (Princeton University Press, 2010).
- [42] Agata, R. *et al.* An adjoint-based simultaneous estimation method of the asthenosphere’s viscosity and afterslip using a fast and scalable finite-element adjoint solver. *Geophysical Journal International* **213**, 461–474 (2018). URL http://dx.doi.org/10.1093/gji/ggx561/oup/backfile/content_public/journal/gji/213/1/10.1093_gji_ggx561/1/ggx561.pdf.
- [43] Miyazaki, H. *et al.* Overview of the k computer system. *Fujitsu Scientific and Technical Journal* **48**, 255–265 (2012).
- [44] Ohzono, M. *et al.* Strain anomalies induced by the 2011 tohoku earthquake (m w 9.0) as observed by a dense gps network in northeastern japan. *Earth, planets and space* **64**, 17 (2012).
- [45] Sato, M. *et al.* Displacement above the hypocenter of the 2011 Tohoku-Oki earthquake. *Science (New York, N.Y.)* **332**, 1395 (2011). URL <http://www.ncbi.nlm.nih.gov/pubmed/21596950>.